Fracture surface topography investigation and fatigue life assessment of notched austenitic steel specimens

Wojciech Macek [a,*], Grzegorz Robak [b], Krzysztof Żak [b], Ricardo Branco [c]

[a] Gdańsk University of Technology, Faculty of Mechanical Engineering and Ship Technology, Gabriela Narutowicza 11/12, 80-233 Gdańsk, Poland
[b] Opole University of Technology, Faculty of Mechanical Engineering, Mikołajczyka 5, 45-271 Opole, Poland
[c] CEMMPRE, Department of Mechanical Engineering, University of Coimbra, Rua Luís Reis Santos, Pinhal de Marrocos, 3030-788 Coimbra, Portugal

ABSTRACT

The objectives of this study were to investigate the fracture surface topography of X8CrNiS18-9 austenitic stainless-steel specimens for different loadings and notch radii and to supplement the knowledge about the fracture mechanisms for fatigue performance. Cases with three different values of the notch radius ρ and the stress amplitude σ_a were analysed. The fracture topographies were quantified by the areas over their entire surfaces with the aid of an optical confocal measurement system. The results showed a well-correlated root mean square height Sq and void volume Vv, identifying the characteristics of the entire fracture method. A fracture surface topography fatigue damage model was developed based on the product of the stress amplitude σ_a by the Sq to the Vv ratio. Overall, the predictions were close to the fatigue lives found in the experiments.

1. Introduction

Developing models for fatigue life assessment of notched components is complex because there are many variables involved in the analysis [1–5]. The stress concentration effect, combined with cyclic stress [6] and strain [7] histories, can cause permanent microstructural changes which are likely to result in fatigue failure. Nevertheless, due to the increasing complexity of current engineering components, geometric discontinuities are inevitable and may introduce complex local stress–strain distributions which are strongly dependent on the notch configuration [8]. Therefore, the development of safe and accurate fatigue design models is one of the main goals of modern industry. Over the last years, different engineering approaches have been proposed. However, until now, there is no universal models, which opens perspectives for the consolidation of new models and new fatigue damage parameters.

Within the most recent proposals, we would like to mention the model introduced by Gao et al. [9] who studied the stress gradient effect on the fatigue life considering the Theory of Critical Distances (TCD) whose key concept is the determination of a critical fatigue quantifier, e.g. stress or strain, nearby the geometric details [10]. They found that the fatigue lives estimated from an effective strain defined using the TCD were in good agreement with the experimental results. Vantadori et al. [11] proposed a criterion for the fatigue life estimation in high-strength steels, in which the influence of non-metallic inclusions was considered. The authors proposed a multiaxial fatigue criterion based on the Carpinteri's model [12] in combination with the $\sqrt{\text{area}}$ model [13]. Their criterion was also found to have satisfactory accuracy. Recent comprehensive review papers on the notch effect and the fatigue life modelling can be found in the references [8,14].

---

* Corresponding author.
E-mail address: wojciech.macek@pg.edu.pl (W. Macek).

Nomenclature

A	definition area (mm^2)
α	opening angle of v-notch (°)
E	Young's modulus (GPa)
K_t	Stress concentration factor (-)
N_{cal}	predicted fatigue life (cycles)
N_f	fatigue life (cycles)
ρ	notch radius (mm)
$σ_a$	stress amplitude (MPa)
$σ_{y02}$	yield stress (MPa)
$σ_u$	ultimate tensile strength (MPa)
$ν$	Poisson's ratio (-)
P	topographic stress factor (MPa)
P_E	prediction error (-)
Ra	arithmetic mean deviation of the roughness profile (mm)
Sa	arithmetical mean height (mm)
Sq	root mean square height (mm)
Sp	maximum peak height (mm)
Sv	maximum pit depth (mm)
Sz	maximum height (mm)
Vv	void volume (mm^3/mm^2)
Vm	material volume (mm^3/mm^2)
Vmc	core material volume (mm^3/mm^2)
Vmp	peak material volume (mm^3/mm^2)
Vvc	core void volume (mm^3/mm^2)
Vvv	pit void volume (mm^3/mm^2)
RMSE	root mean square error
R^2	coefficient of determination
SSE	sum of squared error
SSR	sum of squared regression
SST	total sum of squares

Several fatigue life prediction models based on a variety of factors, sensitive to the loading scenario or the material type, have been proposed. Based on the material sensitivity coefficient, various theories and methods have been developed [15–17]. In addition, various models have been created to account for the loading history [18]. The influence of corrosion as well as the technological treatments of the material are also important factors in design [19–21]. This has motivated the development of alternative methods to deal with these complex effects. For example, Śnieżek et al. [22] examined the influence of the functioning environment on stainless steel fatigue and found semi-elliptical cracks using a measuring technique based on direct-current electrophoretic deposition.

The study of the fatigue crack paths is also extremely important in the case of building materials. This allows to understand whether or not a failure is benign as well as allows to estimate the fatigue crack growth rates [23]. Golewski [24] used the digital image correlation technique for fly ash concrete, which was found to be accurate under mode II fracture and useful for new crack tip tracking. Chapetti [25] developed different fracture mechanics and proved that the critical crack size was related to the fatigue limit variations associated with the loading ratio. An extensive reflection about the advancements in the field of fatigue damage detection measurement techniques are described elsewhere [26]. Robak [27] developed an algorithm for assessing the fatigue life of notched elements by applying the concept of fictitious radius based on the Neuber method. The algorithm considers the variability of the microstructural length, which depends on the number of cycles to failure. The function thus obtained can be used to select the appropriate value for this length, which simplifies the calculation procedure needed to estimate the fatigue life.

Fractographic investigation is a fundamental area of modern engineering which takes place after the fatigue failure of elements [28–31]. In particular, three-dimensional (3D) fractography appears to be a promising field for quantitative analysis [32,33]. Previously reported research showed promising positive results for the field parameters Sx and Vx as well as for the fractal dimension, in the context of the description of fatigue fracture surfaces [34–37]. The fractographic identification of failure events not only provides an in-depth understanding of fracture mechanisms but can also be useful for the development of fatigue life estimation models. The entire fracture surface method [38,39], successfully used in previous studies [38,39], has shown high potential to correlate the fractographic damage with the fatigue loading. However, it has not been applied to fatigue life estimation so far. In this paper, it is introduced a new fracture surface topography fatigue damage model based on the product of the nominal stress amplitude $σ_a$ by the Sq to the Vv ratio. The model is tested in a austenitic stainless steel, and it is expected to be applied to other fatigue cases in the future.

2. Experimental tests

2.1. Fatigue research

The fatigue tests were carried out in a previous research by Robak [27]. The tests were conducted on cylindrical specimens with a circumferential notch (see Fig. 1) manufactured from X8CrNiS18-9 austenitic stainless steel. The basic mechanical properties of the studied material, determined in a previous study [27], were as follows: Young's modulus, E = 200 GPa; offset (0.2%) yield stress, σ_{y02} = 180 MPa; ultimate tensile strength, σ_u = 825 MPa; and Poisson's ratio, ν = 0.31. The experiments were conducted on a tensile-compression hydraulic testing system under constant-amplitude loading. The notch radii in the specimens were 0.2, 0.5, and 0.7 mm, which corresponded to stress concentration factors, K_t, equal to 4.70, 3.09, and 2.67, respectively. Three specimens were used at each loading level. The nominal normal stress amplitudes considered in this research were 160, 220, and 240 MPa. A summary of the fatigue life (N_f) results registered in the experiments for the three combinations of loading levels and notch radii (i.e. nine different cases) is exhibited in Fig. 2. The fatigue life N_f was defined as the number of cycles for which the specimen separated into two pieces, i. e. total failure.

2.2. Fracture surface topography

The fracture surface topographies were recorded using a Sensofar 3D optical profilometer (S-Neox). Measurements were made using the focus variation method at magnifications of five and ten times. This method uses the sharpness of the reflected light surface image with the best focus in an optical microscope to assess the heights of the surface irregularities. The 3D parameters and the 3D visualisation of the treated surfaces were determined using the Digital Surf MountainsMap software. The height parameters Sx and functional parameters (volume) Vx used in the fractographic analysis were calculated according to ISO 25,178 standard. Detailed information about their physical meaning can be found in previous articles [40–43].

In accordance with the entire fracture method, the entire fracture surface of the specimens made of X8CrNiS18-9 austenitic stainless steel was extracted to a circular region of interest (ROI) with a diameter of 8 mm. The Sx parameters used in this research, are the root mean square height Sq, and the arithmetical mean height Sa, defined by the following equations:

$$Sq = \sqrt{\frac{1}{A}\iint_A Z^2(x,y)dx\,dy} \tag{1}$$

$$Sa = \frac{1}{A}\iint_A |z(x,y)|dx\,dy \tag{2}$$

where A is the definition area; z is the surface height in position $\times$, y; x and y are the lengths in the perpendicular directions. The following Sx parameters were also used: maximum pit height Sv defined as the absolute value of the height of the largest pit within the defined area; maximum height Sz that is the height between the highest peak and the deepest valley and the maximum peak height Sp. Fig. 3 shows the calculation of the ISO 25,178 functional volume parameters from the Abbott–Firestone curve. The Vx parameters describe the characteristics of the volume of the appropriate size with respect to the surface area of the surface being examined. Fig. 3a shows the conversion of the region of interest (ROI) into a series of profiles. Fig. 3b presents the volume parameters in relation to the profiles and the Abbott–Firestone curve (blue line).

3. Results

The results of the fatigue tests for the X8CrNiS18-9 austenitic stainless steel, shown in this section, as referred to above, were obtained for three different stress amplitudes σ_a and notch radii ρ. The visualisation of the ROI, together with the results of surface topography measurements, is shown in Fig. 4. For each sample, the fracture surface obtained in the tests, the pseudo-colour view of the surface with the marked ROI, and the values of the surface height Sx and functional Vx parameters are presented sequentially in Fig. 4. In each case, the image under study has been labelled with the value of the obtained fatigue life N_f.
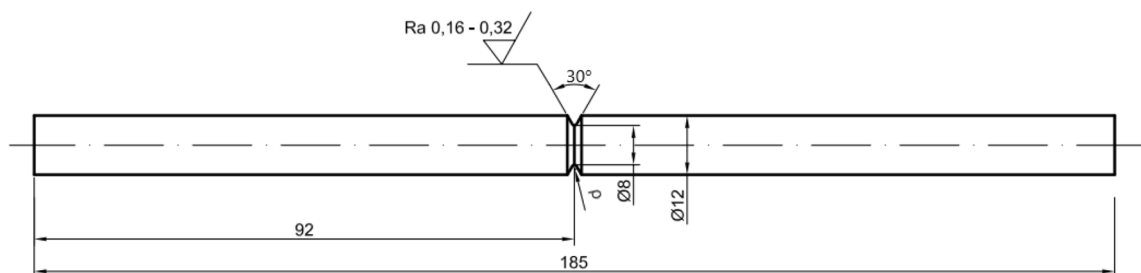

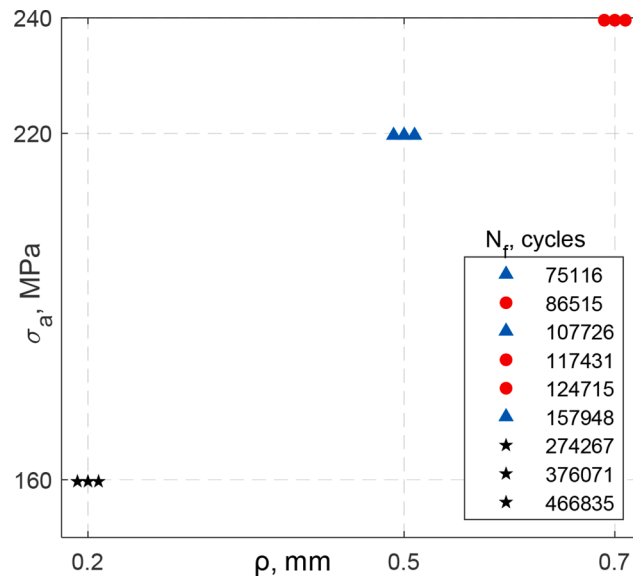**Fig. 1.** Specimen geometry (dimensions in millimetres).

Fig. 2. Stress amplitude σ_a and notch radius ρ, grouped by fatigue life N_f.
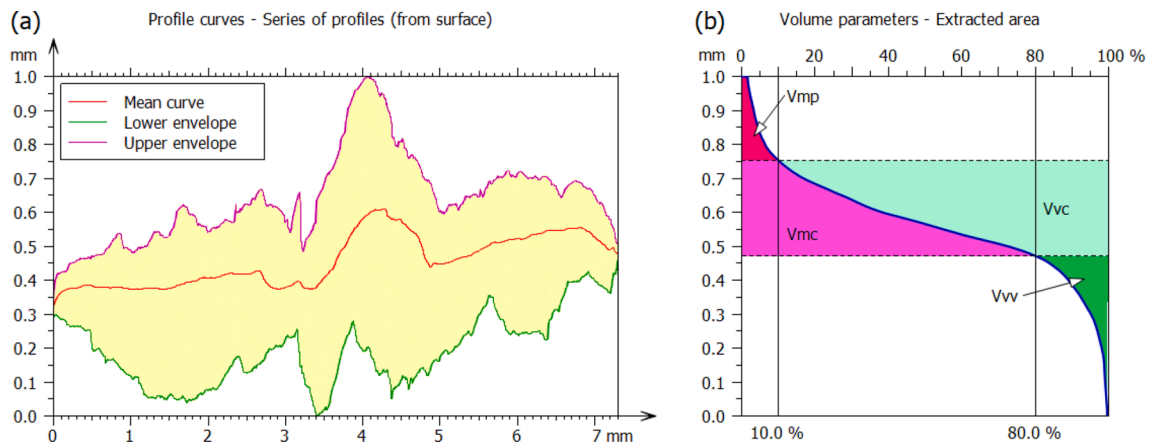

Fig. 3. Graphical presentation of the functional (volume) parameters: (a) series of surface profiles and (b) functional (volume) parameters of the Abbott–Firestone curve according to ISO 25,178 standard.

Fig. 5 presents boxplots showing the dependencies of all analysed surface topography parameters, both the Sx and Vx families, on the notch radius ρ and the stress amplitude σ_a. On each box, the central mark is the median, the edges of the box are the 25th and 75th percentiles, and the whiskers correspond to the most extreme surface topography parameter values. Each box visually represents the measured three Sx and Vx data points for each group ρ (see Fig. 5a) and σ_a (see Fig. 5b). For the notch radius ρ and the stress amplitudes σ_a, the individual parameters followed a similar trend because each σ_a level corresponded to a ρ level. Overall, we can see that the largest scatter of the surface topography parameters (i.e. both Sx and Vx) occurred for the intermediate values, i.e., $\rho = 0.5$ mm and σ_a = 220 MPa (see Fig. 5a and 5b, respectively). The Sq and Vv parameters showed the best fit with respect to notch radius ρ, as demonstrated by the higher correlations of determination R^2 which reached 0.9668 and 0.9859, for cubic fittings, respectively. The same parameters in terms of stress σ_a, also for cubic fitting, showed values of R^2 equal to 0.9489 and 0.9764, respectively.

Fig. 6 presents the scatter plots along with the fit curves generated by the basic fitting function of the MATLAB program (for the best-fitted cases), showing the dependencies of all analysed surface topography parameters (Sx and Vv) on the fatigue life N_f. The N_f - Sx and the N_f - Vx datapoints are represented by the scatter plots with circular markers, while the fitted functions are plotted by the full lines. The coefficient of determination R^2, defined by the following formula:

$$R^2 = \frac{SSR}{SST} = 1 - \frac{SSE}{SST}$$

(3)

where SST = SSR + SSE. SSE is the sum of the squared error, and SSR is the sum of the squared regression, indicates the proportional
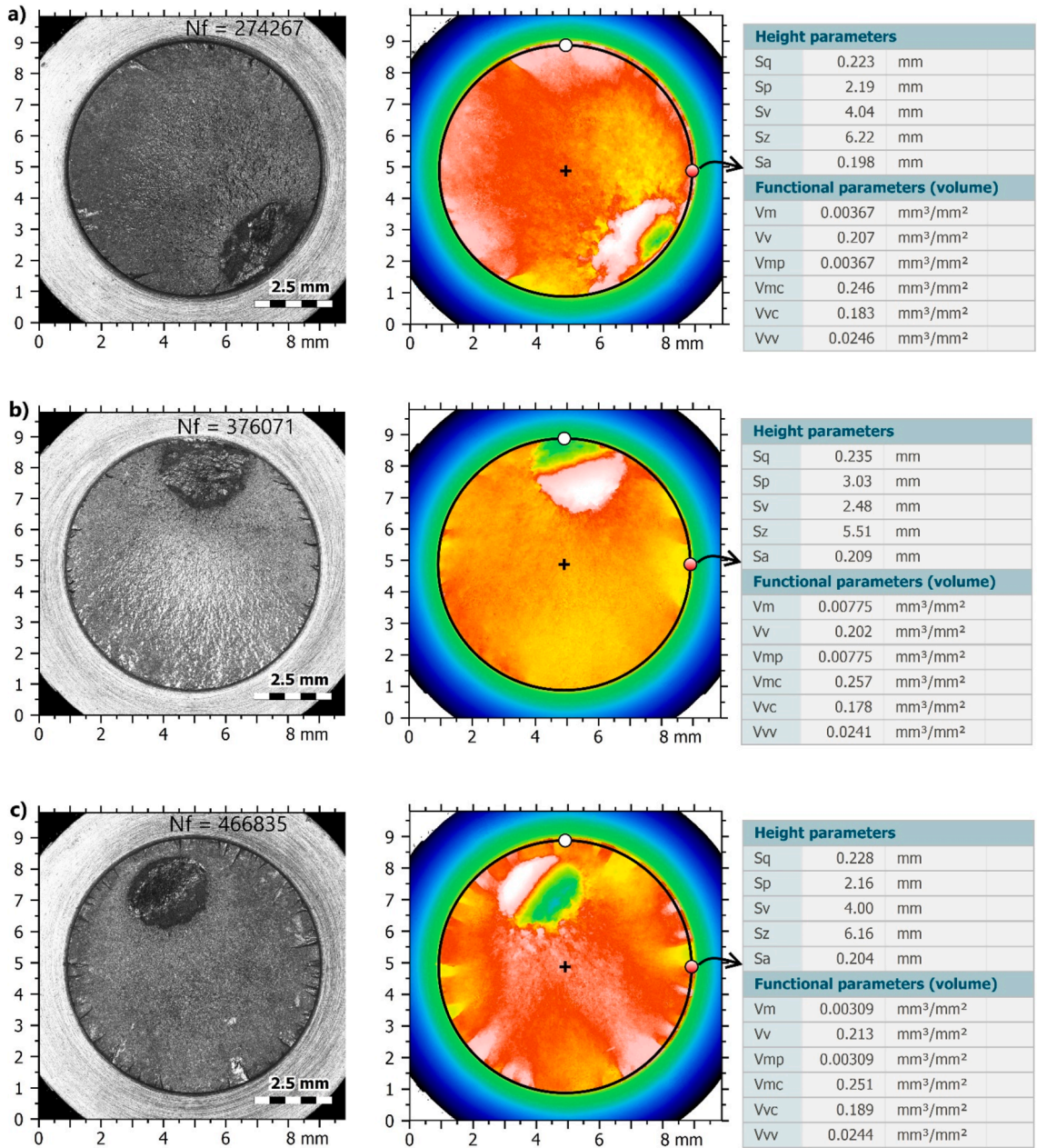
Fig. 4. Visualization of the fracture surfaces with investigated ROIs marked for specimens with (a, b, c) σ_a = 160 MPa and ρ = 0.2 mm, (d, e, f) σ_a = 220 MPa and ρ = 0.5 mm, and (g, h, i) σ_a = 240 MPa and ρ = 0.7 mm.

amount of variation in the response variable Y expressed by the independent variable X in the regression model.

The root mean square height Sq and void volume Vv were the most fitted, and this result was also confirmed by another study [44]. This relationship can be seen in Fig. 5 with respect to (a) the notch radius ρ and (b) the stress amplitude σ_a as well as in Fig. 6 for the fatigue life N_f. The values of both Sq and Vv increase for higher stress amplitudes σ_a and notch radii ρ. However, the aforementioned surface topography parameters decrease with increasing fatigue lives N_f in the cubic fit manner. For higher fatigues lives, the values are relatively similar, while for lower lives there is a significant variation from case to case.
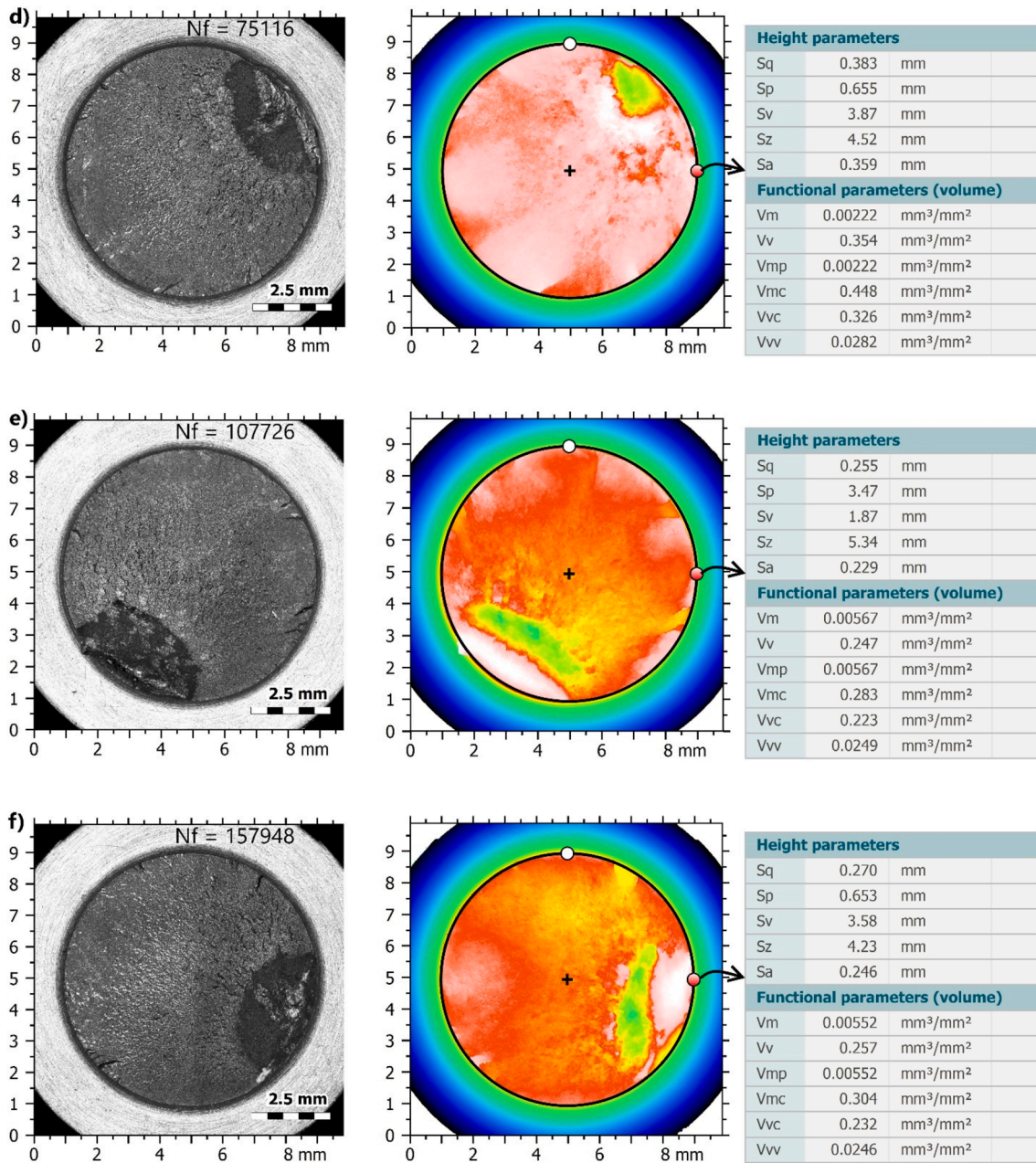
d) Nf = 75116

Height parameters		
Sq	0.383	mm
Sp	0.655	mm
Sv	3.87	mm
Sz	4.52	mm
Sa	0.359	mm
Functional parameters (volume)		
Vm	0.00222	mm³/mm²
Vv	0.354	mm³/mm²
Vmp	0.00222	mm³/mm²
Vmc	0.448	mm³/mm²
Vvc	0.326	mm³/mm²
Vvv	0.0282	mm³/mm²

e) Nf = 107726

Height parameters		
Sq	0.255	mm
Sp	3.47	mm
Sv	1.87	mm
Sz	5.34	mm
Sa	0.229	mm
Functional parameters (volume)		
Vm	0.00567	mm³/mm²
Vv	0.247	mm³/mm²
Vmp	0.00567	mm³/mm²
Vmc	0.283	mm³/mm²
Vvc	0.223	mm³/mm²
Vvv	0.0249	mm³/mm²

f) Nf = 157948

Height parameters		
Sq	0.270	mm
Sp	0.653	mm
Sv	3.58	mm
Sz	4.23	mm
Sa	0.246	mm
Functional parameters (volume)		
Vm	0.00552	mm³/mm²
Vv	0.257	mm³/mm²
Vmp	0.00552	mm³/mm²
Vmc	0.304	mm³/mm²
Vvc	0.232	mm³/mm²
Vvv	0.0246	mm³/mm²

Fig. 4. (*continued*).

4. Discussion

4.1. Fracture surface topography fatigue damage model

The fatigue damage model used is this study is based on the most suitable topography parameters identified in the previous section, i.e. Sq and Vv, as well as on the applied nominal stress amplitude σ_a. In the current approach, a new parameter P (see Eq. (4)), defined from the Sq to Vv ratio multiplied by the stress amplitude σ_a, was introduced. Fig. 7 shows the correlation between the new parameter P and the fatigue life for the tested cases. As can be seen, the results can be fitted by linear functions with a high correlation coefficient, which is an interesting outcome. The fit residuals, as a bar plot, are also displayed in the bottom part of the same figure. The fit residuals are defined as the difference between the ordinate data point and the resulting fit for each abscissa data point. This subplot also shows the result for the norm of residuals which is a measure of the goodness of fit, where a smaller value indicates a better fit than a bigger value. Apart from the good correlation between the new parameter P and the fatigue life N_f, the additional advantage of such an
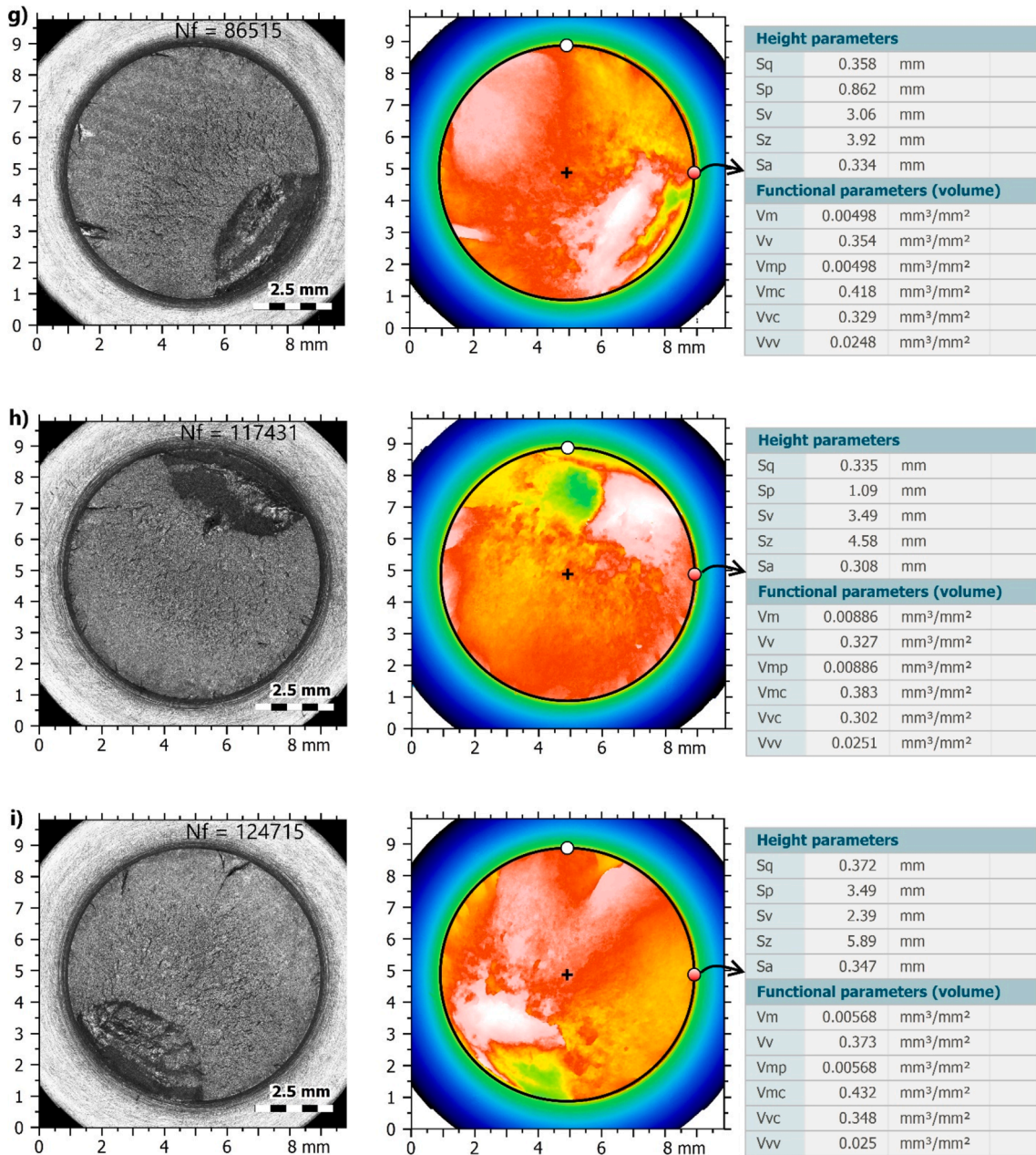
g)

Height parameters		
Sq	0.358	mm
Sp	0.862	mm
Sv	3.06	mm
Sz	3.92	mm
Sa	0.334	mm
Functional parameters (volume)		
Vm	0.00498	mm³/mm²
Vv	0.354	mm³/mm²
Vmp	0.00498	mm³/mm²
Vmc	0.418	mm³/mm²
Vvc	0.329	mm³/mm²
Vvv	0.0248	mm³/mm²

h)

Height parameters		
Sq	0.335	mm
Sp	1.09	mm
Sv	3.49	mm
Sz	4.58	mm
Sa	0.308	mm
Functional parameters (volume)		
Vm	0.00886	mm³/mm²
Vv	0.327	mm³/mm²
Vmp	0.00886	mm³/mm²
Vmc	0.383	mm³/mm²
Vvc	0.302	mm³/mm²
Vvv	0.0251	mm³/mm²

i)

Height parameters		
Sq	0.372	mm
Sp	3.49	mm
Sv	2.39	mm
Sz	5.89	mm
Sa	0.347	mm
Functional parameters (volume)		
Vm	0.00568	mm³/mm²
Vv	0.373	mm³/mm²
Vmp	0.00568	mm³/mm²
Vmc	0.432	mm³/mm²
Vvc	0.348	mm³/mm²
Vvv	0.025	mm³/mm²

Fig. 4. (*continued*).

approach is that it considers the topography of the fracture surface directly, and accounts for indirectly the notch radius without the need of an explicit modelling of the stress gradient at the notch root, which is one of the underlying concepts of several current fatigue design approaches.

$$P = \frac{Sq}{Vv}\sigma_a \qquad (4)$$

The observed fatigue life N_f and the predicted fatigue life N_{cal} computed from the fracture surface parameter model (see Eq. (5)) is compared in Fig. 8. As can be seen, the calculations are very well correlated with the experimental lives, regardless of the stress amplitude and the notch radius. It is clear that all datapoints are within scatter bands with factors of 1.5 and are placed either in the conservative side or in the unconservative side. In the same figure, the present results are compared to the predictions obtained by Robak [27], for the same cases, which were based on the concept of fictious radius, as explained in Section 1. In this second approach, the datapoints are shifted to the right side of the figure, i.e. the conservative region but are more distant from the experimental lives
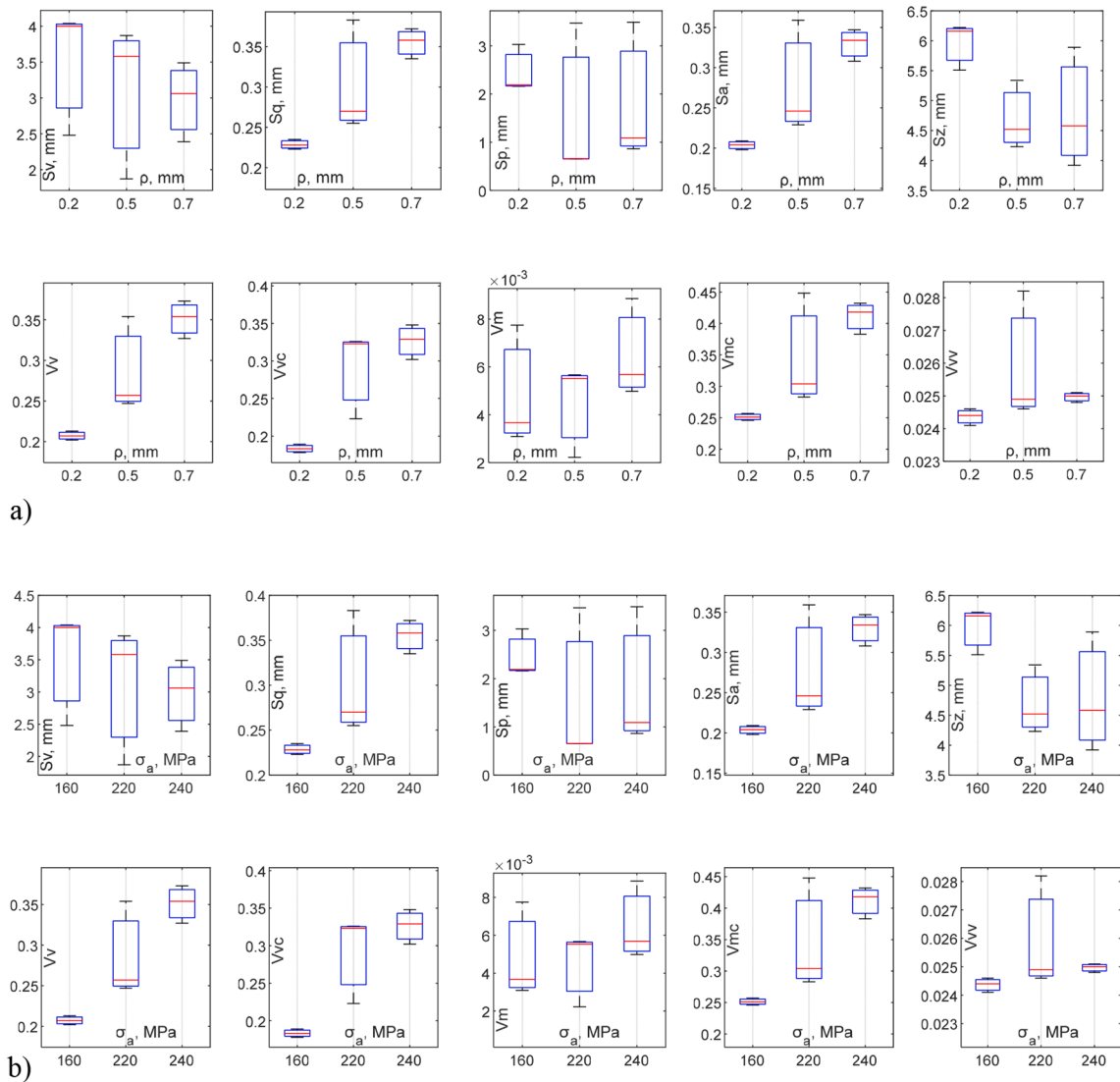
Fig. 5. Boxplots for height Sx and functional Vx surface parameters versus (a) notch radius ρ and (b) stress amplitude σ$_a$.

than the former approach.

$$N_f = -4132 \times P + 1.094 \times 10^6 \tag{5}$$

A more effective evaluation of the predictive capabilities of both models can be carried out via a statistical study that accounts for the probability density functions based in the prediction error P$_E$, defined as follows:

$$P_E = \text{Log}(N_f) - \text{Log}(N_{cal}) \tag{6}$$

where N$_f$ is the observed fatigue life, and N$_{cal}$ is the calculated fatigue life. The best model is generally the one that ensures lower values of the standard deviation and mean errors closer to zero. As far as can be seen in Fig. 9, the proposed model captures well both the notch effect and the loading scenario, because the mean errors are quite almost zero (see Table 1) and the standard deviations are slightly smaller (see Table 1) than that of the model of reference [27]. As already anticipated in Fig. 8, the model based on the fictitious radius is more conservative than that of the present study.

Table 1 presents some statistical values computed from the N$_f$/N$_{cal}$ ratios for the tested cases, namely the maximum and minimum values, the standard deviations, the variances, and also the mean deviations. For the model presented in this paper, the minimum and maximum values of the N$_f$/N$_{cal}$ ratio are equal to −0.1737 and 0.1680, respectively, which are almost symmetrical. In the case of the model based on the fictitious radius, not surprisingly, both values are positive, i.e. 0.0729 and 0.4808, respectively, which confirms its conservative nature. Regarding the variance, it can be seen that the values are relatively similar for both predictive approaches, respectively equal to 0.0155 for the presented model, and 0.0184 for the other approach.
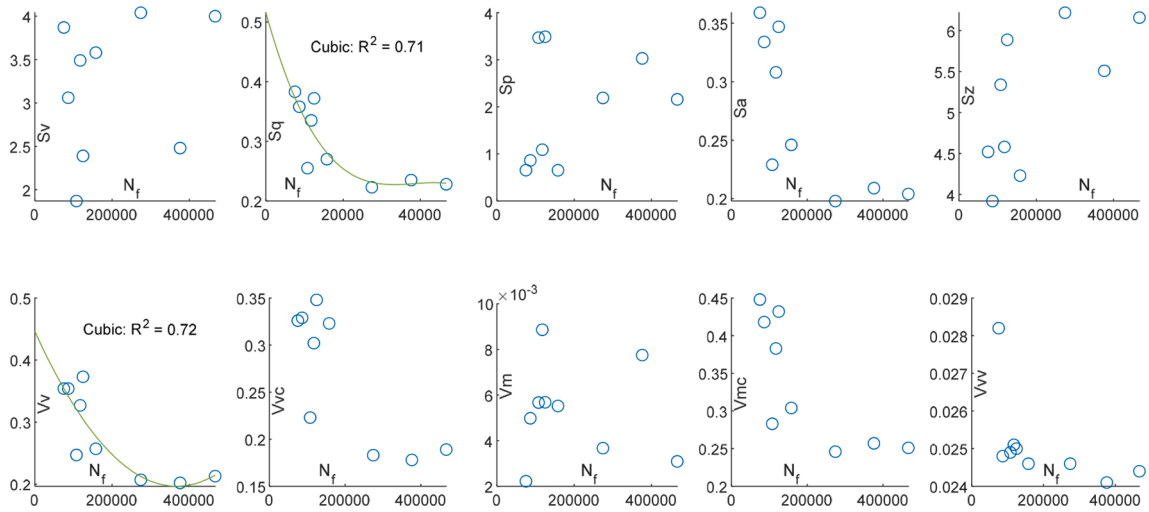
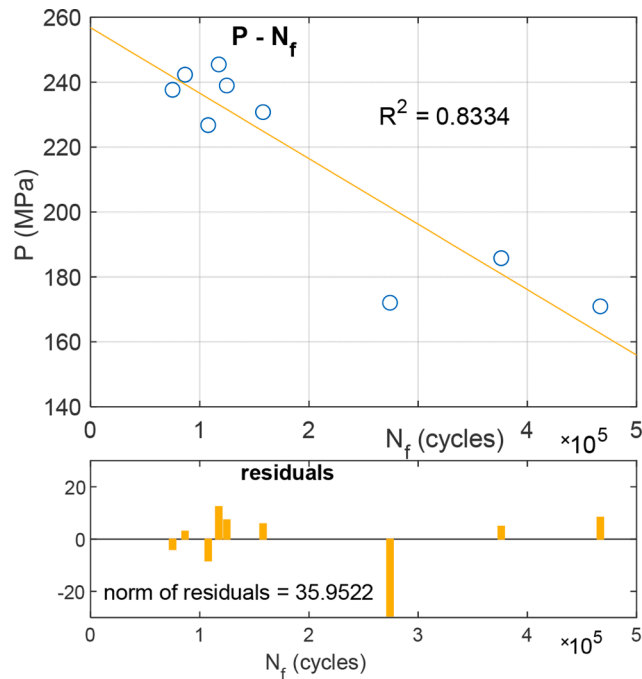**Fig. 6.** Scatter plots for fatigue life N_f versus Sx and Vx parameters.

Fig. 7. Topographic stress factor P versus fatigue life N_f with a linear fit.

4.2. Observation of fracture zones

Fig. 10a and 10b show three characteristic views of the fatigue fracture surface representative of the initiation, propagation, and final rupture regions for the specimen with the highest and the lowest fatigue life. Fig. 10a shows the fracture surface formation characteristics of the X8CrNiS18-9 austenitic stainless steel fatigued at a stress amplitude σ_a of 160 MPa and notch radius of $\rho = 0.2$ mm. Fig. 10b shows the surface damage topography of the specimens fatigued at a stress amplitude of $\sigma_a = 220$ MPa and notch radius of $\rho = 0.5$ mm.

For the specimen with the highest N_f value (see Fig. 10a), a large number of cracks can be observed around the circumference of the sample which denotes a multi-crack initiation process. As a result, deeper valleys in the initiation area can be found which is not visible in the propagation area. In contrast, for the lowest fatigue life case (see Fig. 10b), the roughness of the surface increases with the decrease of the distance to the rupture region, which can be explained by the increase of the fatigue crack growth rates as the crack grows. In both analysed cases, it is clear that the initiation area has a small number of deep furrows while the propagation area is more
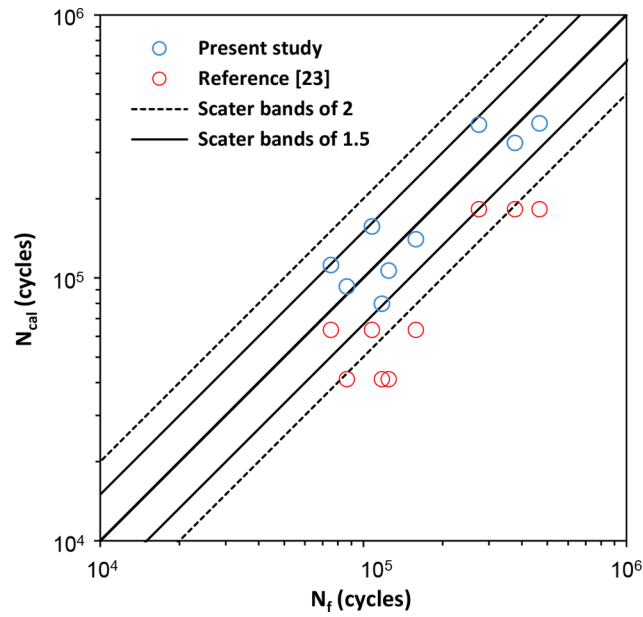
9

Fig. 8. Comparison of the predicted fatigue lives N_{cal} and the observed fatigue lives N_f: dashed lines represent a scatter band of 2, while the thin full lines represent a scatter band of 1.5.
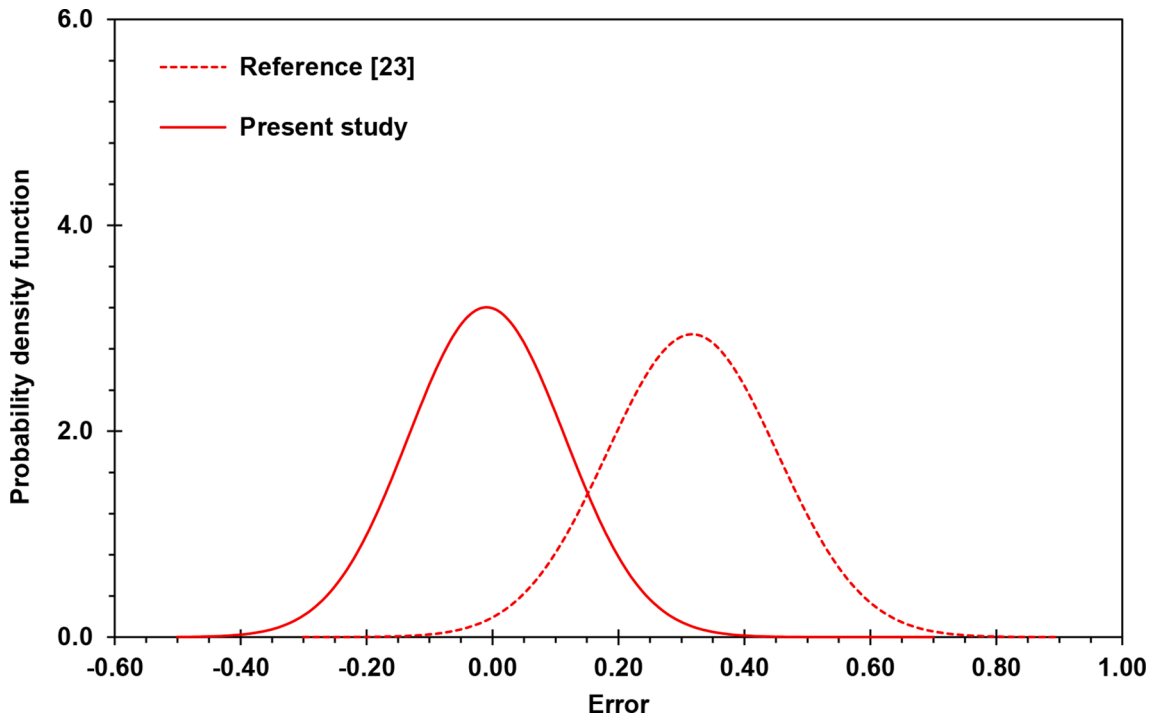

Fig. 9. Probability density functions defined from the predictive error for both fatigue life prediction models considered in this study.
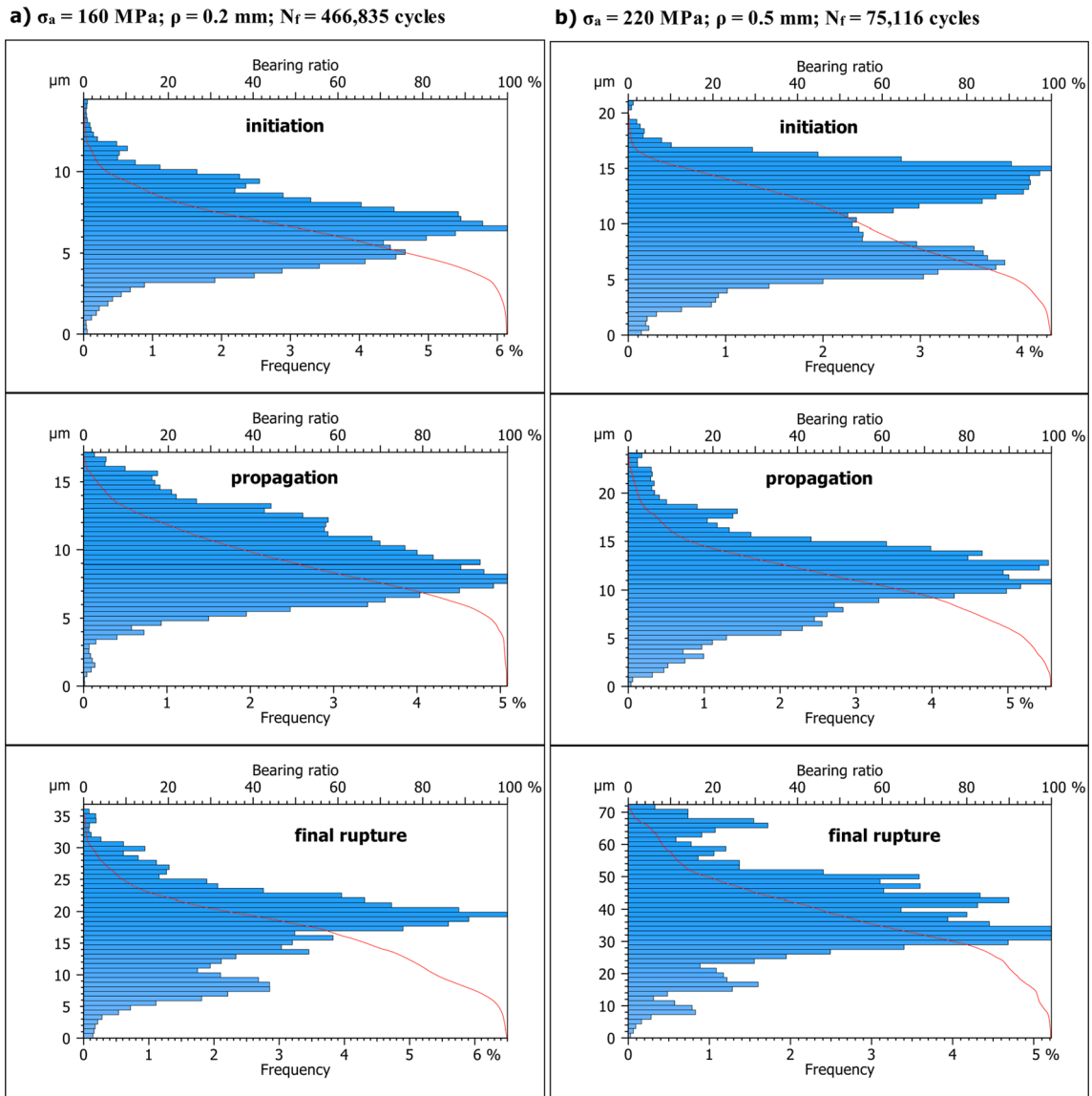
Table 1
Statistical values of the fatigue life prediction models.

Model	Mean deviation	Standard deviation	Variance	Minimum N_f/N_{cal}	Maximum N_f/N_{cal}
Present study	−0.0093	0.1245	0.0155	−0.1737	0.1680
Reference [27]	0.31715	0.1356	0.0184	0.0729	0.4808

σ_a = 160 MPa; ρ = 0.2 mm; N_f = 466,835 cycles

σ_a = 220 MPa; ρ = 0.5 mm; N_f = 75,116 cycles
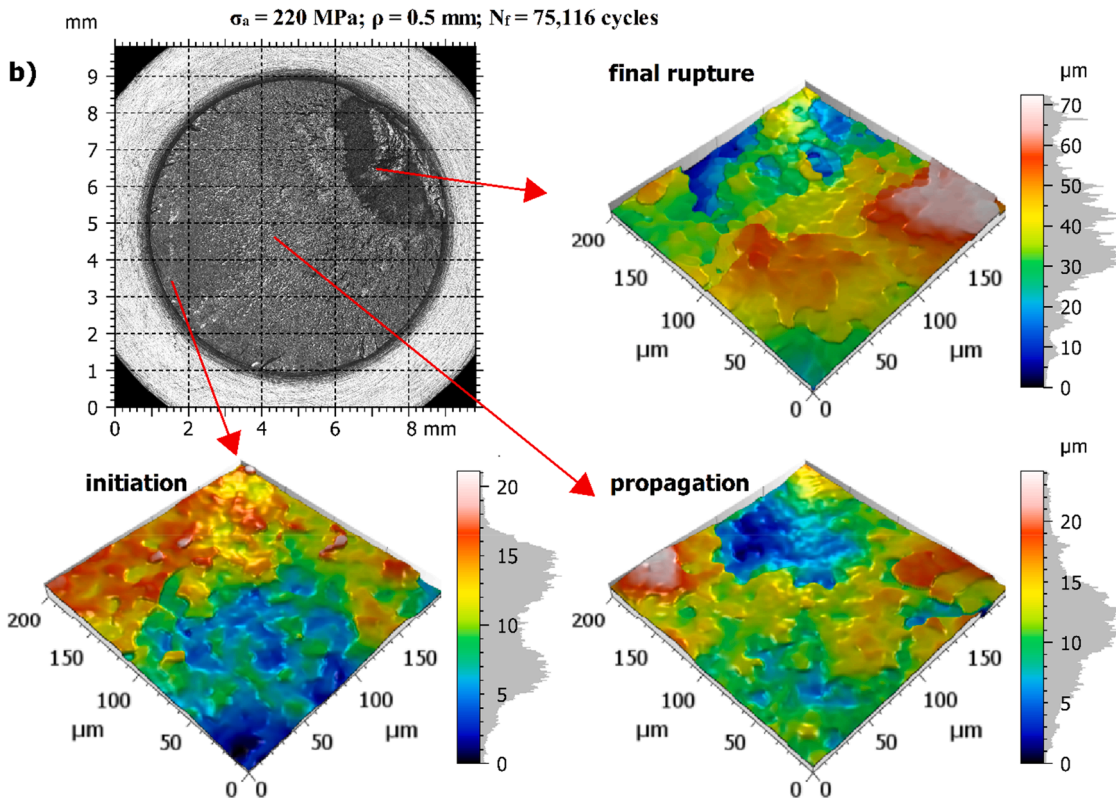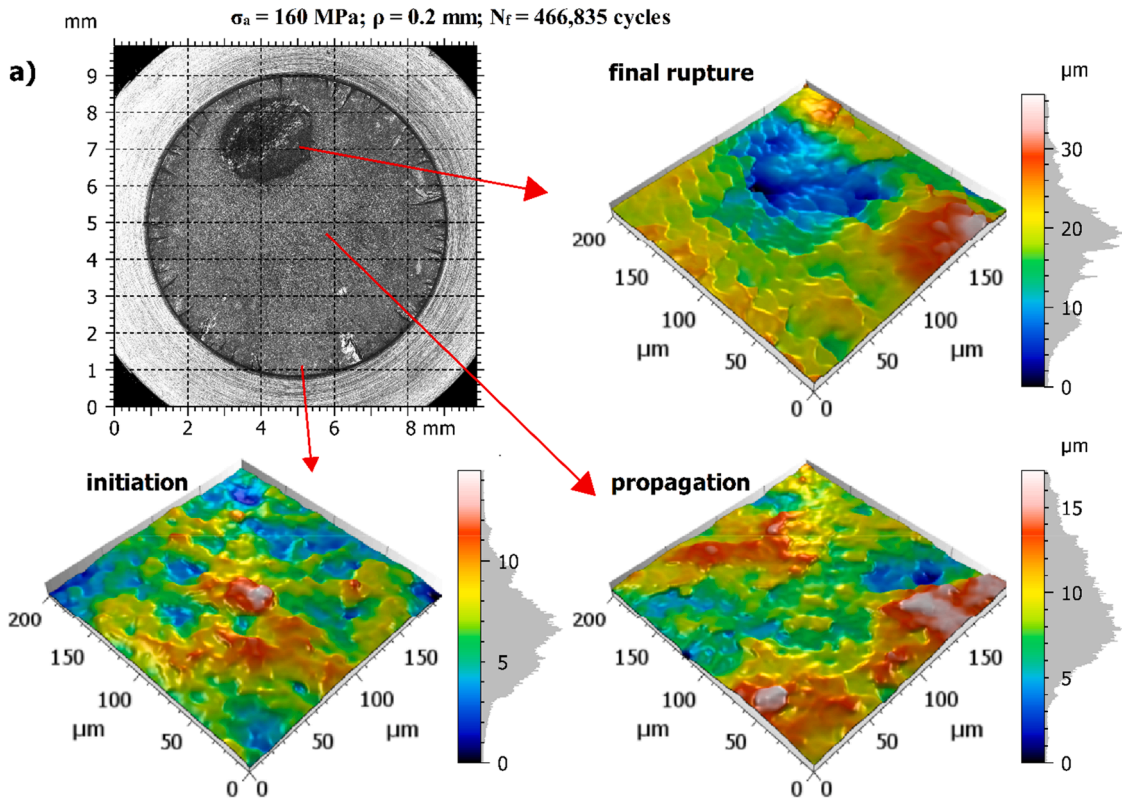
(caption on next page)

Fig. 10. Characteristic zones of selected fatigue fractures: (a) highest (N_f = 466,835 cycles; σ_a = 160 MPa; ρ = 0.2 mm) and (b) lowest N_f (N_f = 75,116 cycles; σ_a = 220 MPa; ρ = 0.5 mm) fatigue life.

a) σ_a = 160 MPa; ρ = 0.2 mm; N_f = 466,835 cycles   **b)** σ_a = 220 MPa; ρ = 0.5 mm; N_f = 75,116 cycles

Fig. 11. Height histograms and Abbott curves for initiation, propagation and final rupture zones: (a) highest (N_f = 466,835 cycles; σ_a = 160 MPa; ρ = 0.2 mm) and (b) lowest N_f (N_f = 75,116 cycles; σ_a = 220 MPa; ρ = 0.5 mm) fatigue life specimens.

even with smaller valleys.

A more quantitative analysis of the surface roughness variations can be done by means of the so-called Abbott-Firestone curves. Fig. 11 plots both the histograms, represented in blue, which allow to observe the height distribution, and the Abbott-Firestone curves, represented in red, which shows the cumulating function of the depth distribution. As can be seen, widths of each bin are 0.3 μm to 1.4 μm, depending on the height, and the number of bins is always 50 in total for each histogram. It is interesting to note, as expected, that initiation zones are characterised by the smallest values of height distribution, which tend to increase for the propagation and rupture areas. Comparing the plots for extreme fatigue lives, we can find higher values of the height distribution for the smallest fatigue life, which can be explained by the highest fatigue crack growth rates.

The examination of fracture surfaces by scanning electron microscopy (SEM) can provide interesting clues on the failure mechanisms. Fig. 12 displays the micrographs taken with a Tescan Vega 4 microscope for the specimens with the highest fatigue life (N_f = 466,835 cycles; σ_a = 160 MPa; ρ = 0.2 mm) and lowest fatigue life (N_f = 75,116 cycles; σ_a = 220 MPa; ρ = 0.5 mm). For each case,
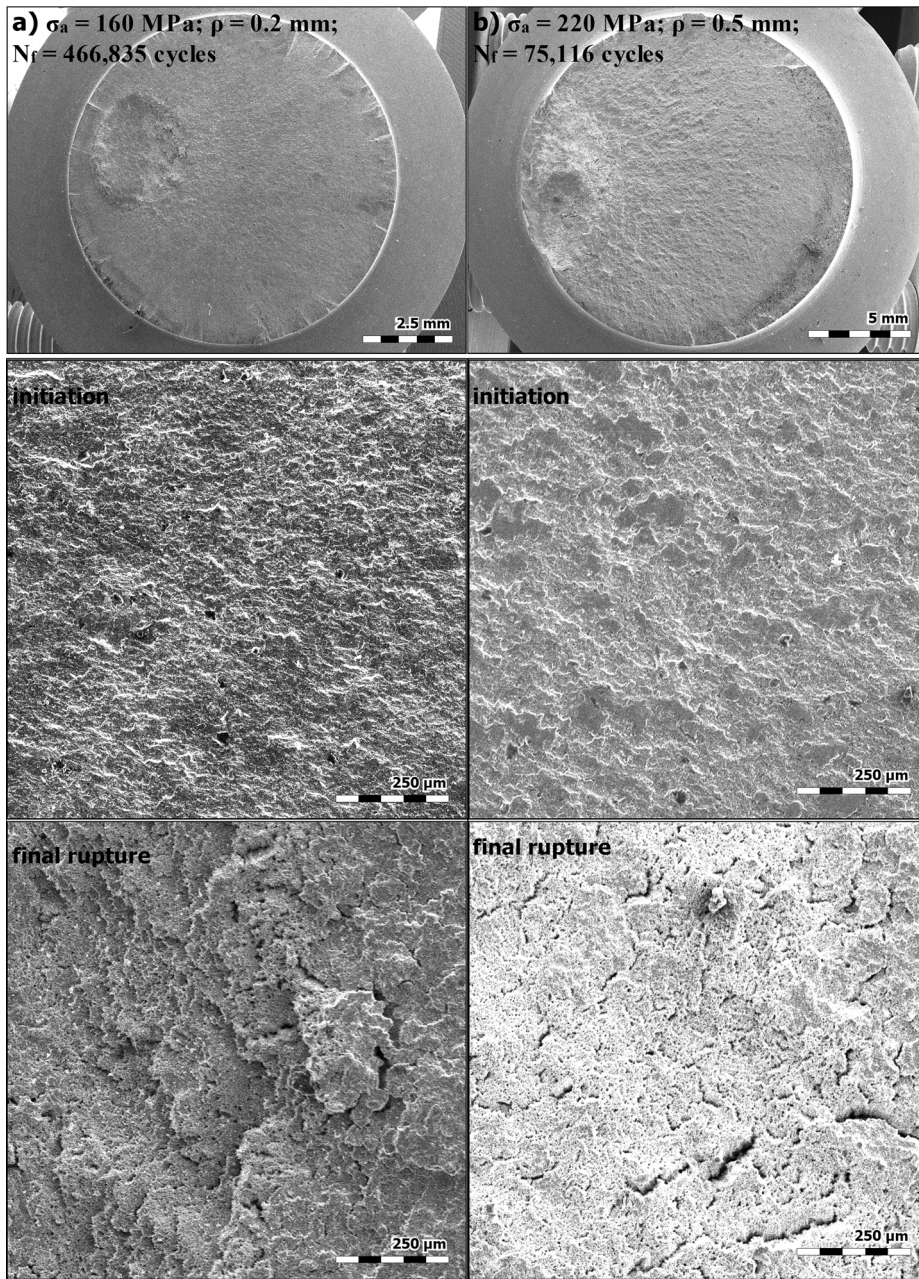
Fig. 12. SEM fractography for initiation and final rupture zones: (a) highest (N_f = 466,835 cycles; σ_a = 160 MPa; ρ = 0.2 mm) and (b) lowest N_f (N_f = 75,116 cycles; σ_a = 220 MPa; ρ = 0.5 mm) fatigue life specimens.

views of the entire fracture surface as well as cropped (1 mm × 1 mm) areas from the initiation and final rupture zones are shown. At the initiation sites, there is clear evidence of plastic deformation marked on fracture surfaces, which is typical fatigue loading and denotes smaller fatigue crack growth rates. As the cracks propagate, the surfaces present obvious cleavage fracture characteristics, with many narrow cleavage facets distributed along the direction of the crack growth. For the final fracture zone, standard cleavage fracture with secondary microcracks was found.

5. Conclusions

The present paper demonstrated that the post failure application of fracture surface measurements is beneficial for investigating the fatigue life and the fatigue damage accumulation in notched specimens subjected to severe stress gradient effects. Based on the studied X8CrNiS18-9 austenitic stainless steel specimens, the following conclusions can be drawn:

- The analysis of the fracture surface parameters (Sq and Vv) with the entire fracture area method showed that their values increase with higher values of the stress amplitude σ_a and the notch radius ρ, and decrease with an increase in the fatigue life N_f;
- The relationship between the topographic stress factor P and the fatigue life N_f led to a good correlation than between both variables, regardless of the notch radius and the stress amplitude, allowing to account for the stress gradients and the load scenarios directly from the fracture surface analysis, without the need of a explicitly modelling of the notch effect;
- The proposed fracture surface topography fatigue damage model based on the topographic stress factor P, defined from Sq to Vv ratio multiplied by the stress amplitude, was capable to predict the fatigue life, accommodating implicitly the notch effect and the associated stress gradients;
- The analysis of the surface topography of the fracture characteristic zones (i.e. initiation, propagation, and final rupture zones) confirmed that the lowest roughness was observed in the initiation zone, while the highest roughness was found in the final rupture zone except in the places with deep furrows.

The proposed fatigue life prediction model, developed in the light of the entire fracture area method, opens new perspectives in the post-mortem characterisation of mechanical failures, allowing the correlation between the fatigue life and fracture surface topography characteristics in specimens subjected to severe stress gradients. Currently, the model has been successfully applied to high-strength steels subjected to uniaxial loading. Its main limitation is the fact that it requires the entire fracture surface which may hinder its application to engineering components with partial failure. In the future, other geometries, including smooth and notch configurations, as well as other engineering materials and loading scenarios will be evaluated for compliance with the fracture surface criterion defined by the new topographic stress factor P.

Declaration of Competing Interest

The authors declare that they have no known competing financial interests or personal relationships that could have appeared to influence the work reported in this paper.

Acknowledgments

References

[1] R. Branco, J.D. Costa, L.P. Borrego, F. Berto, S.M.J. Razavi, W. Macek, Comparison of different one-parameter damage laws and local stress-strain approaches in multiaxial fatigue life assessment of notched components, Int. J. Fatigue. 151 (2021) 106405, https://doi.org/10.1016/j.ijfatigue.2021.106405.
[2] A. Carpinteri, A. Spagnoli, S. Vantadori, D. Viappiani, A multiaxial criterion for notch high-cycle fatigue using a critical-point method, Eng. Fract. Mech. 75 (7) (2008) 1864–1874, https://doi.org/10.1016/j.engfracmech.2006.11.002.
[3] D. Liao, S.-P. Zhu, G. Qian, Multiaxial fatigue analysis of notched components using combined critical plane and critical distance approach, Int. J. Mech. Sci. 160 (2019) 38–50, https://doi.org/10.1016/j.ijmecsci.2019.06.027.
[4] T. Łagoda, G. Robak, J. Słowik, Fatigue life of steel notched elements including the complex stress state, Mater. Des. 51 (2013) 935–942, https://doi.org/10.1016/j.matdes.2013.04.087.
[5] G. Robak, T. Łagoda, Variability of fatigue parameters under uniaxial loading in the function of the number of cycles to failure, Int. J. Fatigue. 113 (2018) 246–252, https://doi.org/10.1016/J.IJFATIGUE.2018.04.003.
[6] P. Zhao, F.Z. Xuan, C. Wang, A physically-based model of cyclic responses for martensitic steels with the hierarchical lath structure under different loading modes, J. Mech. Phys. Solids. 124 (2019) 555–576, https://doi.org/10.1016/J.JMPS.2018.11.006.
[7] H. Zhang, Q. Wang, X. Gong, T. Wang, Y. Pei, W. Zhang, Y. Liu, C. Wang, Q. Wang, Comparisons of low cycle fatigue response, damage mechanism, and life prediction of MarBN steel under stress and strain-controlled modes, Int. J. Fatigue. 149 (2021) 106291, https://doi.org/10.1016/j.ijfatigue.2021.106291.
[8] D. Liao, S.-P. Zhu, J.A.F.O. Correia, A.M.P. De Jesus, F. Berto, Recent advances on notch effects in metal fatigue: A review, Fatigue & Fracture of Eng. Mat. Structures. 43 (4) (2020) 637–659.
[9] D. Gao, W. Yao, W. Wen, J. Huang, Critical distance model for the fatigue life analysis under low-velocity impacts of notched specimens, Int. J. Fatigue. 146 (2021) 106164, https://doi.org/10.1016/j.ijfatigue.2021.106164.
[10] D. Taylor, Geometrical effects in fatigue: a unifying theoretical model, Int. J. Fatigue. 21 (5) (1999) 413–420, https://doi.org/10.1016/S0142-1123(99)00007-9.
[11] S. Vantadori, C. Ronchei, D. Scorza, A. Zanichelli, L.C. Araújo, J.A. Araújo, Influence of non-metallic inclusions on the high cycle fatigue strength of steels, Int. J. Fatigue. 154 (2022) 106553, https://doi.org/10.1016/j.ijfatigue.2021.106553.
[12] A. Carpinteri, C. Ronchei, D. Scorza, S. Vantadori, Critical Plane Orientation Influence on Multiaxial High-Cycle Fatigue Assessment, Phys. Mesomech. 18 (4) (2015) 348–354, https://doi.org/10.1134/S1029959915040074.
[13] Y. Murakami, Metal fatigue: Effects of small defects and nonmetallic inclusions, Met. Fatigue Eff. Small Defects Nonmet. Inclusions. (2019) 1–758, https://doi.org/10.1016/C2016-0-05272-5.
[14] M. Kamal, M.M. Rahman, Advances in fatigue life modeling: A reviewRenewable and Sustainable Energy Reviews. 82 (2018) 940–949, https://doi.org/10.1016/J.RSER.2017.09.047.
[15] Ł. Pejkowski, D. Skibicki, Stress-strain response and fatigue life of four metallic materials under asynchronous loadings: Experimental observations, Int. J. Fatigue. 128 (2019) 105202, https://doi.org/10.1016/j.ijfatigue.2019.105202.
[16] L. Molent, A. Spagnoli, A. Carpinteri, R. Jones, Using the lead crack concept and fractal geometry for fatigue lifing of metallic structural components, Int. J. Fatigue. 102 (2017) 214–220, https://doi.org/10.1016/J.IJFATIGUE.2017.04.001.
[17] A. Tomczyk, A. Seweryn, Experimental investigation and modeling of damage accumulation of EN-AW 2024 aluminum alloy under creep condition at elevated temperature, Materials (Basel). 14 (2021) 1–17, https://doi.org/10.3390/ma14020404.
[18] A. Karolczuk, K. Kluger, T. Łagoda, A correction in the algorithm of fatigue life calculation based on the critical plane approach, Int. J. Fatigue. 83 (2016) 174–183, https://doi.org/10.1016/J.IJFATIGUE.2015.10.011.
[19] D. Peng, C. Tang, N. Matthews, R. Jones, S. Kundu, R.K.S. Raman, A. Alankar, Computing the Fatigue Life of Cold Spray Repairs to Simulated Corrosion Damage, Materials 14 (16) (2021) 4451, https://doi.org/10.3390/ma14164451.

[20] M.B. Djukic, V. Sijacki Zeravcic, G.M. Bakic, A. Sedmak, B. Rajicic, Hydrogen damage of steels: A case study and hydrogen embrittlement model, Eng. Failure Analysis 58 (2015) 485–498, https://doi.org/10.1016/j.engfailanal.2015.05.017.

[21] A. Janeczek, J. Tomków, D. Fydrych, The Influence of Tool Shape and Process Parameters on the Mechanical Properties of AW-3004 Aluminium Alloy Friction Stir Welded Joints, Materials 14 (12) (2021) 3244, https://doi.org/10.3390/ma14123244.

[22] L. Śniezek, T. Ślezak, K. Grzelak, V. Hutsaylyuk, An experimental investigation of propagation the semi-elliptical surface cracks in an austenitic steel, Int. J. Press. Vessel. Pip. 144 (2016) 35–44, https://doi.org/10.1016/J.IJPVP.2016.05.006.

[23] A. Carpinteri, Part-through cracks in round bars under cyclic combined axial and bending loading, Int. J. Fatigue. 18 (1) (1996) 33–39.

[24] G.L. Golewski, Measurement of fracture mechanics parameters of concrete containing fly ash thanks to use of Digital Image Correlation (DIC) method, Measurement. 135 (2019) 96–105, https://doi.org/10.1016/J.MEASUREMENT.2018.11.032.

[25] M.D. Chapetti, Fracture mechanics for fatigue design of metallic components and small defect assessment, Int. J. Fatigue. 154 (2022) 106550, https://doi.org/10.1016/j.ijfatigue.2021.106550.

[26] F. Bjørheim, S.C. Siriwardane, D. Pavlou, A review of fatigue damage detection and measurement techniques, Int. J. Fatigue. 154 (2022) 106556, https://doi.org/10.1016/j.ijfatigue.2021.106556.

[27] G. Robak, Using a variable value of the fictitious radius to estimate fatigue life of notched elements, Fatigue Fract. Eng. Mater. Struct. 43 (9) (2020) 2006–2023, https://doi.org/10.1111/ffe.13280.

[28] C.R.F. Azevedo, A.H. Feller, Selected cases of failure analysis and the regulatory agencies in Brazil. Part 1: Aviation, railway and health, Eng. Fail. Anal. 97 (2019) 354–373, https://doi.org/10.1016/J.ENGFAILANAL.2019.01.003.

[29] M. Fonte, V. Infante, L. Reis, M. Freitas, Failure mode analysis of a diesel motor crankshaft, Eng. Fail. Anal. 82 (2017) 681–686, https://doi.org/10.1016/j.engfailanal.2017.06.010.

[30] R. Masoudi Nejad, F. Berto, Fatigue fracture and fatigue life assessment of railway wheel using non-linear model for fatigue crack growth, Int. J. Fatigue. 153 (2021) 106516, https://doi.org/10.1016/j.ijfatigue.2021.106516.

[31] A. Gryguc, S.B. Behravesh, S.K. Shaha, H. Jahed, M. Wells, B. Williams, X. Su, Low-cycle fatigue characterization and texture induced ratcheting behaviour of forged AZ80 Mg alloys, Int. J. Fatigue. 116 (2018) 429–438, https://doi.org/10.1016/J.IJFATIGUE.2018.06.028.

[32] E. Merson, A.V. Kudrya, V.A. Trachenko, D. Merson, V. Danilov, A. Vinogradov, The Use of Confocal Laser Scanning Microscopy for the 3D Quantitative Characterization of Fracture Surfaces and Cleavage Facets, Procedia Struct. Integr. 2 (2016) 533–540, https://doi.org/10.1016/J.PROSTR.2016.06.069.

[33] H. Lauschmann, K. Tesař, K. Jiroušková, Quantitative fractography of fatigue cracks: a new solution in 3D, Procedia Struct. Integr. 23 (2019) 107–112, https://doi.org/10.1016/J.PROSTR.2020.01.071.

[34] W. Macek, Z. Marciniak, R. Branco, D. Rozumek, G.M. Królczyk, A fractographic study exploring the fracture surface topography of S355J2 steel after pseudo-random bending-torsion fatigue tests, Measurement. 178 (2021) 109443, https://doi.org/10.1016/j.measurement.2021.109443.

[35] W. Macek, R. Branco, M. Korpyś, T. Łagoda, Fractal dimension for bending–torsion fatigue fracture characterisation, Measurement. 184 (2021) 109910, https://doi.org/10.1016/j.measurement.2021.109910.

[36] W. Macek, R. Branco, J.D. Costa, C. Pereira, Strain sequence effect on fatigue life and fracture surface topography of 7075–T651 aluminium alloy, Mech. Mater. 160 (2021) 103972, https://doi.org/10.1016/j.mechmat.2021.103972.

[37] W. Macek, Fracture surface formation of notched 2017A–T4 aluminium alloy under bending fatigue, Int. J. Fract. 2021 (2021) 1–17, https://doi.org/10.1007/S10704-021-00579-Y.

[38] W. Macek, Post-failure fracture surface analysis of notched steel specimens after bending-torsion fatigue, Eng. Fail. Anal. 105 (2019) 1154–1171, https://doi.org/10.1016/j.engfailanal.2019.07.056.

[39] W. Macek, Fractal analysis of the bending-torsion fatigue fracture of aluminium alloy, Eng. Fail. Anal. 99 (2019) 97–107, https://doi.org/10.1016/j.engfailanal.2019.02.007.

[40] W. Macek, R. Branco, J. Trembacz, J.D. Costa, J.A.M. Ferreira, C. Capela, Effect of multiaxial bending-torsion loading on fracture surface parameters in high-strength steels processed by conventional and additive manufacturing, Engineering Failure Analysis. 118 (2020) 104784, https://doi.org/10.1016/j.engfailanal.2020.104784.

[41] P. Podulka, The Effect of Surface Topography Feature Size Density and Distribution on the Results of a Data Processing and Parameters Calculation with a Comparison of Regular Methods, Materials 14 (15) (2021) 4077, https://doi.org/10.3390/ma14154077.

[42] International Organisation of Standardization, ISO 25178, Geom. Prod. Specif. – Surf. Texture Areal. (2010).

[43] W. Macek, Correlation between Fractal Dimension and Areal Surface Parameters for Fracture Analysis after Bending-Torsion Fatigue, Metals 11 (11) (2021) 1790, https://doi.org/10.3390/met11111790.

[44] W. Macek, Fracture Areas Quantitative Investigating of Bending-Torsion Fatigued Low-Alloy High-Strength Steel, Metals 11 (10) (2021) 1620, https://doi.org/10.3390/met11101620.